Distributed Full Waveform Inversion in the Frequency Domain for Seismic Networks

Ban-Sok Shin, *Member, IEEE,* and Dmitriy Shutin, *Senior Member, IEEE*

Abstract—We address the problem of frequency-domain seismic imaging in a distributed manner within a network of seismic receivers. This is particularly relevant for future planetary missions, where a multi-agent network is expected to autonomously and cooperatively explore an unknown subsurface by leveraging data exchange among connected agents. To achieve this, we integrate the adapt-then-combine technique into full waveform inversion (FWI) in the frequency domain. Our proposed method enables distributed imaging by requiring connected receivers to exchange both gradients and subsurface models. We evaluate its performance using numerical experiments on synthetic subsurface models, including the Marmousi model. Our results demonstrate that the proposed approach produces high-resolution, accurate subsurface images across all receivers, regardless of their sampling positions. Moreover, the reconstructed images closely match those obtained from traditional, centralized FWI, indicating that our method successfully replicates centralized imaging performance across the receiver network through cooperative data exchange.

Index Terms—Full waveform inversion, seismic imaging, multi-agent seismic exploration, distributed imaging

I. INTRODUCTION

Future space missions will likely employ multiple robotic agents for diverse exploration tasks. One such task is the exploration of the shallow subsurface of a planet, e.g., Moon or Mars, to find and image structures such as lava tubes or caves [1], [2], [3]. Finding such structures is of high interest to the space community since they usually provide an environment with stable temperature and one that is shielded from radiation. Thus, they are promising locations to store space equipment or to even shelter astronauts.

In this respect, we envision the use of autonomous multi-agent systems where each robotic agent is equipped with a geophone to collect seismic measurements on the surface [4]. Furthermore, the agents are connected via wireless links to each other building a communication network that enables data exchange among the agents. In such an application, measurement data are distributed over the agents and a central processing entity might not be available since the system has to conduct the exploration independently. Hence, to enable autonomy of the system distributed data processing is required that leverages communication among the agents. With respect to the task of subsurface imaging, this means that the imaging has to be performed in a distributed fashion, i.e., the agents

exchange and process data such that each agent obtains an estimate of the subsurface image locally. Based on the local subsurface images an exploration strategy can be developed that dictates where the agents should perform new measurements to e.g., obtain an enhanced subsurface image.

In this work, we consider full waveform inversion (FWI) in the frequency domain as the imaging technique that shall be performed in a distributed fashion within a seismic network. FWI is a high-resolution imaging technique that exploits wave physics to image subsurface structures with respect to material parameters such as wave velocity or density. It has been applied to various other domains such as ultrasound, ground penetrating radar (GPR) or electrical resistivity tomography (ERT) [5], [6], [7]. However, in its traditional form it is a centralized method, i.e., it requires all measurement data at a central unit that performs the inversion.

In terms of decentralized imaging techniques in seismic networks some works have been proposed, cf. [8], [9], [10]. However, all these works do not provide fully distributed imaging since either they rely on sink nodes that acts as a central data collector or require a full mesh topology. In contrast to enable fully *distributed imaging*, we proposed several methods in the time domain that provide each agent/receiver in a seismic network with a subsurface image via cooperation, cf. [11]. To enhance the distributed imaging performance and to allow for inversion of single frequencies, in this work we derive a distributed FWI in the frequency domain. Although our work focuses on seismic data, the FWI is versatile such that our method can be easily transferred to other modalities such as ultrasound imaging, GPR or ERT.

II. FULL WAVEFORM INVERSION IN FREQUENCY DOMAIN

In the following, we give a brief review of FWI in the frequency domain. While in time domain the wave equation is employed, in frequency domain the Helmholtz equation serves as the corresponding forward operator. Solving the Helmholtz equation provides us with a wavefield for a specific frequency ω over spatial coordinate $\mathbf{x}$. For a source function $f_s(\omega, \mathbf{x})$ the Helmholtz equation is given as

$$\Delta u_s(\mathbf{x}, \omega) + \omega^2 m(\mathbf{x}) u_s(\mathbf{x}, \omega) = f_s(\mathbf{x}, \omega), \qquad (1)$$

where s indicates the respective source function and Δ is the Laplacian operator. The wavefield is denoted by $u_s(\mathbf{x}, \omega)$ over spatial coordinate $\mathbf{x}$ and angular frequency ω and $m(\mathbf{x})$ is the spatial distribution of squared slowness in the subsurface. The source function $f_s(\mathbf{x}, \omega)$ models external excitation, e.g. strikes or explosions. We employ second-order Clayton-Enquist absorbing boundaries in the spatial domain to reduce

unwanted reflections from the domain boundaries [12]. Applying finite differences to the Helmholtz equation results in a system of linear equations:

$$\mathbf{A}(\omega, \mathbf{m})\mathbf{u}_s(\omega, \mathbf{m}) = \mathbf{f}_s(\omega) \qquad (2)$$

Matrix $\mathbf{A}(\omega, \mathbf{m})$ encodes finite difference approximations of the Helmholtz equation. It has a banded structure, is complex and usually sparse. Assuming a total of $N_\mathrm{x}N_\mathrm{z}$ grid cells after discretization of the computational domain, matrix $\mathbf{A}(\omega)$ has dimensions $N_\mathrm{x}N_\mathrm{z} \times N_\mathrm{x}N_\mathrm{z}$. The wavefield vector $\mathbf{u}_s(\omega, \mathbf{m})$ and the source vector $\mathbf{f}_s(\omega)$ contain wavefield samples and respective source function values over the complete computational domain such that $\mathbf{u}(\omega, \mathbf{m}) \in \mathbb{C}^{N_\mathrm{x}N_\mathrm{z}}$ and $\mathbf{f}_s(\omega) \in \mathbb{C}^{N_\mathrm{x}N_\mathrm{z}}$, respectively. To obtain correct source function values, the time-series of the source function needs to be transformed to the frequency domain via Fourier transform and the complex source amplitude needs to be picked for the considered frequency ω. To solve (2) with respect to $\mathbf{u}_s(\omega)$, we use the generalized minimal residual method (GMRES) which is an efficient iterative sparse solver for linear equation systems.

In seismic imaging, we are interested in estimating the squared slowness $m(\mathbf{x})$ in the subsurface. To this end, an inverse problem needs to be solved, in FWI a highly nonlinear and non-convex one. This is achieved by minimizing a cost functional with respect to the slowness vector $\mathbf{m}(\mathbf{x})$. The optimization problem in FWI for N_S sources is then formulated as follows:

$$\min_{\mathbf{m}} \mathcal{J}(\mathbf{m}) = \frac{1}{2}\sum_{\omega}\sum_{s=1}^{N_\mathrm{S}} || \underbrace{\mathbf{P}^\mathsf{T}\mathbf{u}_s(\omega, \mathbf{m})}_{\mathbf{d}_s^{\mathrm{syn}}(\omega, \mathbf{m})} - \mathbf{d}_s^{\mathrm{obs}}(\omega) ||_2^2 \quad (3a)$$

$$\text{s.t.} \quad \mathbf{A}(\omega, \mathbf{m})\mathbf{u}_s(\omega, \mathbf{m}) = \mathbf{f}_s(\omega) \qquad (3b)$$

Problem (3a) is constrained by the Helmholtz equation (3b) since synthesized data $\mathbf{d}_s^{\mathrm{syn}}(\omega, \mathbf{m})$ needs to adhere to it. Matrix $\mathbf{P} \in \mathbb{R}^{N_\mathrm{x}N_\mathrm{z} \times N_\mathrm{R}}$ is a sampling operator that extracts synthesized/predicted data $\mathbf{d}_s^{\mathrm{syn}}(\omega, \mathbf{m})$ from the computed wavefield $\mathbf{u}_s(\omega, \mathbf{m})$ at the receiver positions. FWI employs gradient-based optimization to find a solution for $\mathbf{m}(\mathbf{x})$. To obtain the gradient of $\mathcal{J}(\mathbf{m})$ wrt. $\mathbf{m}$ the adjoint-state method is applied [13]. This method allows the computation of the gradient of a cost functional that is constrained by a PDE. Applying the adjoint-state method results in the following computation of the gradient:

$$\nabla_{\mathbf{m}}\mathcal{J}(\mathbf{m}) = \mathrm{Re}\left\{ \sum_{\omega}\sum_s \omega^2 \boldsymbol{\lambda}_s^*(\omega, \mathbf{m}) \odot \mathbf{u}_s(\omega, \mathbf{m}) \right\} \quad (4)$$

where $*$ denotes complex conjugate of the matrix entries, $\odot$ denotes element-wise multiplication and $\boldsymbol{\lambda}_s(\omega) \in \mathbb{C}^{N_\mathrm{x}N_\mathrm{z}}$ is the discretized adjoint-state wavefield. To obtain $\boldsymbol{\lambda}_s(\omega)$, the following system of linear equations needs to be solved for each source s:

$$\mathbf{A}^\mathsf{H}(\omega, \mathbf{m})\boldsymbol{\lambda}_s(\omega, \mathbf{m}) = \mathbf{P}^\mathsf{T}\mathbf{u}_s(\omega, \mathbf{m}) - \mathbf{d}_s^{\mathrm{obs}}(\omega). \quad (5)$$

In essence, (5) solves the Helmholtz equation again but for an adapted forward operator and now with the data residuals $\mathbf{u}_s(\omega, \mathbf{m}) - \mathbf{d}_s^{\mathrm{obs}}(\omega)$ placed at the receiver positions. These residuals are now back-propagated through the subsurface

$\mathbf{m}(\mathbf{x})$ to give the adjoint wavefield. Now, using the gradient $\nabla_{\mathbf{m}}\mathcal{J}(\mathbf{m})$ we can update the slowness values $\mathbf{m}$ iteratively e.g. by gradient-descent:

$$\mathbf{m}^{[k+1]} = \mathbf{m}^{[k]} + \alpha^{[k]}\nabla_{\mathbf{m}}\mathcal{J}(\mathbf{m})|_{\mathbf{m}=\mathbf{m}^{[k]}}. \quad (6)$$

The update procedure can be conducted by other optimization schemes such as nonlinear conjugate gradient or L-BFGS.

The cost in (3) has multiple local minima due to the cycle-skipping problem of FWI [14]. Hence, during iterative optimization FWI is prone to fall into a local minimum that does not accurately describe the subsurface. To overcome this issue, one common approach is to start the inversion with low frequency data and then continually increase the considered frequency. This strategy stems from the fact that the cost $\mathcal{J}(\mathbf{m})$ is known to have less local minima in the low frequency regime [15].

III. Frequency Domain Adapt-Then-Combine Full Waveform Inversion

In the following section we will introduce a distributed full waveform inversion scheme that computes subsurface images at each receiver via cooperation. We start by describing the network model and then derive our proposed method.

A. Seismic network model

For the seismic network we assume an array of N_R seismic receivers or geophones positioned in a line topology. Each receiver r has a set of neighbors $\mathcal{N}_r$ that consists of those receivers ℓ that can exchange data with receiver r and vice versa including receiver r itself. Furthermore, we assume that the topology graph is connected, i.e., there is a multi-hop connection between any two receivers in the network and the network graph is not separated.

B. Proposed method

Our goal in distributed subsurface imaging is to obtain a subsurface image close to the centralized image at each receiver locally via cooperation. This needs to be achieved via data exchange among neighboring receivers only. To this end, we adopt the adapt-then-combine (ATC) methodology from distributed linear estimation in sensor networks [16]. First, we separate the global cost in (3a) into N_R local cost functions over the receivers:

$$\mathcal{J}(\mathbf{m}) = \sum_r \mathcal{J}_r(\mathbf{m}) \qquad (7)$$

with

$$\mathcal{J}_r(\mathbf{m}) = \frac{1}{2}\sum_{\omega}\sum_s |\mathbf{p}_r^\mathsf{T}\mathbf{u}_s(\omega, \mathbf{m}) - d_{s,r}^{\mathrm{obs}}(\omega)|^2. \quad (8)$$

Since each receiver will reconstruct its own subsurface image, we assign individual subsurface models $\mathbf{m}_r \in \mathbb{R}^{N_\mathrm{x}N_\mathrm{z}}$ to each receiver $r = 1, \ldots, N_\mathrm{R}$. This will affect the local cost which now depends on the receiver-specific image $\mathbf{m}_r$, i.e., $\mathcal{J}_r(\mathbf{m}_r)$. It is important to note, that now each receiver needs to solve the Helmholtz equation for its own subsurface model $\mathbf{m}_r$ which results in receiver-specific wavefields $\mathbf{u}_{s,r}(\omega, \mathbf{m}_r)$

indicated by the subscript r. Based on its local cost $\mathcal{J}_r(\mathbf{m}_r)$ each receiver r computes a local gradient using the adjoint-state method:

$$\delta\mathbf{m}_r = \mathrm{Re}\left\{\sum_\omega \sum_s \omega^2 \boldsymbol{\lambda}_{s,r}^*(\omega, \mathbf{m}_r) \odot \mathbf{u}_{s,r}(\omega, \mathbf{m}_r)\right\}. \quad (9)$$

To compute $\delta\mathbf{m}_r$ we need the receiver-specific adjoint wave-field $\boldsymbol{\lambda}_{s,r}$. To this end, each receiver solves the adjoint-state equation using its local data residual analogous to (5):

$$\mathbf{A}^{\mathsf{H}}(\omega, \mathbf{m}_r)\boldsymbol{\lambda}_{s,r}(\omega, \mathbf{m}_r) = \mathbf{p}_r^{\mathsf{T}}\mathbf{u}_{s,r}(\omega, \mathbf{m}_r) - d_{s,r}^{\mathrm{obs}}(\omega) \quad (10)$$

To apply the ATC technique to FWI each receiver needs to exchange its gradient $\delta\mathbf{m}_r$ and subsurface model $\mathbf{m}_r$ with neighboring receivers $\ell \in \mathcal{N}_r$. Then, per iteration k the following computations need to be performed at each receiver r:

$$\text{(Adapt)} \quad \widetilde{\mathbf{m}}_r^{[k+1]} = \mathbf{m}_r^{[k]} + \alpha^{[k]} \sum_{\ell \in \mathcal{N}_r} a_{\ell r} \delta\mathbf{m}_\ell^{[k]} \quad (11a)$$

$$\text{(Combine)} \quad \mathbf{m}_r^{[k+1]} = \sum_{\ell \in \mathcal{N}_r} b_{\ell r} \widetilde{\mathbf{m}}_\ell^{[k+1]} \quad (11b)$$

The coefficients $a_{\ell r}$ and $b_{\ell r}$ are used to weight contributions of gradients and subsurface models within the neighborhood set individually to guarantee convergence of all receivers to a suitable subsurface model. For convergence of the ATC method they need to satisfy certain criteria as described in [16]. In our case, we select them to be $a_{\ell r} = b_{\ell r} = 1/|\mathcal{N}_r|, \forall \ell \in \mathcal{N}_r$ which guarantees convergence to similar subsurface models over all receivers in the network.

The first step (11a) is the so-called adapt step where each receiver fuses gradients from its neighbors and performs a gradient-descent update. After that, intermediate estimates $\widetilde{\mathbf{m}}_r^{[k+1]}$ are exchanged among the receivers and the combine step (11b) is performed which fuses these estimates to give an updated subsurface estimate. This process is repeated iteratively and results in estimates that resemble the classical, centralized FWI result for all receivers.

Remark: In (9) the gradient is computed as a superposition over multiple frequencies ω. However, it is also possible to iterate over single frequencies using FWI. It is common to start inverting low frequencies first to obtain rough structures of the subsurface and after that, higher frequencies which allow to resolve finer details in the image [15]. Doing so, avoids FWI to fall into a local minimum that does not resemble the true subsurface model. In our work, we apply this strategy and hence, we compute a single gradient for each frequency such that no superposition over multiple frequencies is required.

IV. Numerical Results

For numerical evaluation we analyze imaging performance of FD-ATCFWI to the centralized FWI for multiple receivers. As performance measure we use the normalized mean square error (NMSE) which is computed as an average over all grid cells between the true model $\mathbf{m}^\star$ and the estimated one $\mathbf{m}_r^{[k]}$ per iteration k: $\mathrm{NMSE}^{[k]} = \frac{1}{N_{\mathrm{x}}N_{\mathrm{z}}} \cdot ||\mathbf{m}^\star - \mathbf{m}_r^{[k]}||^2/||\mathbf{m}^\star||^2$. For our evaluations we use a nonlinear conjugate gradient step in the model updates (11a) and (6) instead of gradient descent for a more stable convergence.

Algorithm 1 FD-ATCFWI for single frequency

1: Initialize starting models $\mathbf{m}_r^{[0]}, r = 1, \ldots, N_{\mathrm{R}}$
2: Select frequency ω, set $k = 0$
3: **while** iteration $k < N_{\mathrm{FWI}}$ **do**
4:     **for all** receivers $r \leftarrow 1, N_{\mathrm{R}}$ **do**
5:         Get wavefields $\{\mathbf{u}_{s,r}\}_{s=1}^{N_{\mathrm{S}}}$ with (2)
6:         Get adjoint fields $\{\boldsymbol{\lambda}_{s,r}\}_{s=1}^{N_{\mathrm{S}}}$ with (10)
7:         Get local gradient with (9)
8:         Update model $\widetilde{\mathbf{m}}_r^{[k+1]}$ with (11a)
9:         Fuse models to get $\mathbf{m}_r^{[k+1]}$ with (11b)
10:    **end for**
11: **end while**
12: **return** Subsurface images $\mathbf{m}_r^{[N_{\mathrm{FWI}}]}, r = 1, \ldots N_{\mathrm{R}}$

A. Two ellipses

As first subsurface model we consider two elliptic anomalies with different velocities $v_1 = 1.8\,\mathrm{km\,s}^{-1}$ and $v_2 = 1.6\,\mathrm{km\,s}^{-1}$ in a spatial domain of $1.4\,\mathrm{km} \times 0.5\,\mathrm{km}$. These anomalies are embedded into a background model with increasing velocity over depth. The space is discretized with a grid spacing of $\Delta x = \Delta z = 10\,\mathrm{m}$. We initialize both FWI and FD-ATCFWI with that background model only. Furthermore, we employ $N_{\mathrm{R}} = 24$ receivers and $N_{\mathrm{S}} = 20$ sources that are evenly spread over the surface. Each receiver has a maximum of three neighbors to its left- and its right-hand-side with whom it can exchange gradients and slowness models. As source signal we use a Ricker wavelet with dominant frequency $f_{\mathrm{dom}} = 6\,\mathrm{Hz}$ and select frequencies to be in the range of 2 to $8\,\mathrm{Hz}$ with a frequency step of $\Delta f = 1\,\mathrm{Hz}$. For each single frequency we perform $N_{\mathrm{FWI}} = 50$ iterations for both FWI and FD-ATCFWI and use the obtained slowness model as initial model for the next frequency. The step size starts at $\alpha^{[0]} = 0.01$ and is exponentially decreased over the iterations to enable convergence of the estimated subsurface model.

Figure 1 depicts the imaging results obtained by FD-ATCFWI as well as FWI. For FD-ATCFWI, we show the imaging results at three different receivers. One can clearly observe that FD-ATCFWI reconstructs the true model accurately for different receivers. The reconstructed slowness models share high similarity among each other demonstrating convergence of each receiver to a similar subsurface model. Compared to centralized FWI we observe high similarity as well. This demonstrates that we are able to obtain accurate imaging results in a purely distributed fashion without relying on a central entity. Fig. 2 depicts the cost function $\mathcal{J}(\mathbf{m})$ and NMSE over the iteration. For FD-ATCFWI we also depicts performance for a full mesh topology. In terms of the cost function, both FD-ATCFWI and FWI perform close to each other with FWI achieving lower costs due to centralized processing. Since every 50 iterations the respective frequency is changed, a jump can be observed in the cost that gradually decreases over the iterations indicating convergence to a suitable subsurface model. Regarding NMSE performance, we observe that FD-ATCFWI performs close to centralized FWI with an NMSE gap of only 0.01 in the later iterations. This gap is reduced for the case of a full mesh network
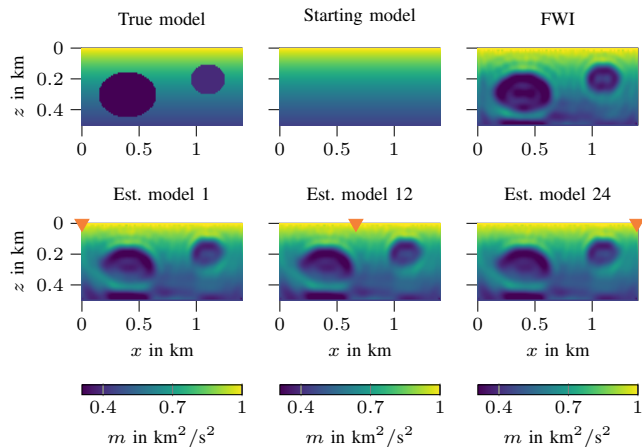
Fig. 1: First row: True model, starting model and FWI result for two ellipses. Second row: Results by FD-ATCFWI with respctive receiver position ▼.
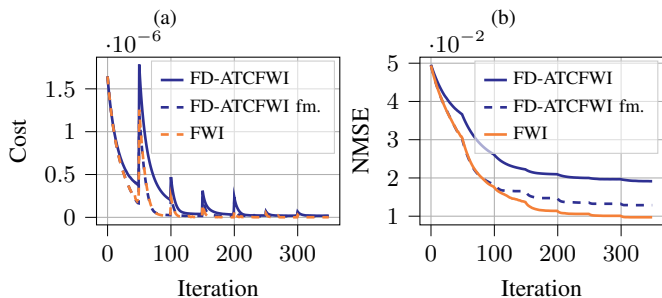

Fig. 2: (a) Cost and (b) NMSE performance of FD-ATCFWI, FD-ATCFWI with full mesh and FWI for two ellipses.

Fig. 3: Imaging results of FD-ATCFWI for varying no. of exchange intervals with receiver position ▼ for two ellipses.

Fig. 4: (a) Cost and (b) NMSE performance of FD-ATCFWI for different no. of exchange intervals.

indicating that with higher connectivity imaging performance of FD-ATCFWI is improved.

B. FD-ATCFWI with reduced data exchange

FD-ATCFWI requires data exchanges among neighboring receivers in each iteration k. Since gradients and local estimates of subsurface models need to be exchanged each receiver needs to transmit $2N_xN_z$ scalar numbers per iteration k to its neighbors. This number depends on the size of the spatial domain which is determined by the physical domain and the selected cell sizes $\Delta x, \Delta z$. For our example of two ellipses we have $N_x = 140, N_z = 50$. Using a float64 representation of the scalar numbers, we obtain $2N_xN_z8$ B/iteration $= 112$ kB/iteration for each receiver in the network. If we allow one iteration, e.g., to take 0.2 s this results in a data rate of 560 kB/s which is fairly low for an uncompressed data transfer. However, if we require a higher spatial resolution and/or lower time for data exchanges, this number quickly increases. Furthermore, with a high number of sampling nodes transmitting data, the communication network can be overloaded by the amount of shared data.

To reduce the amount of shared data within the network, we can reduce the interval of data exchanges among the receivers in FD-ATC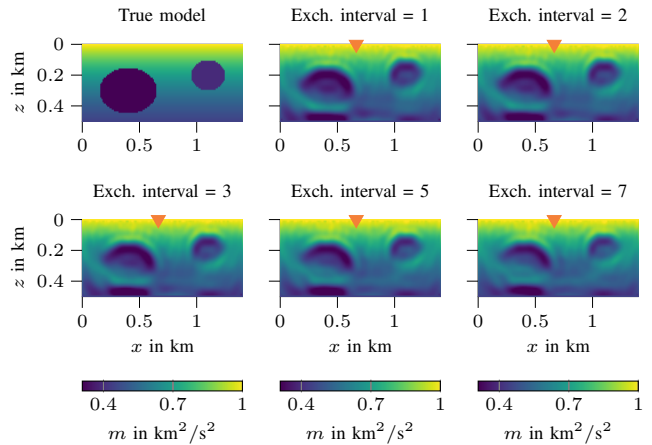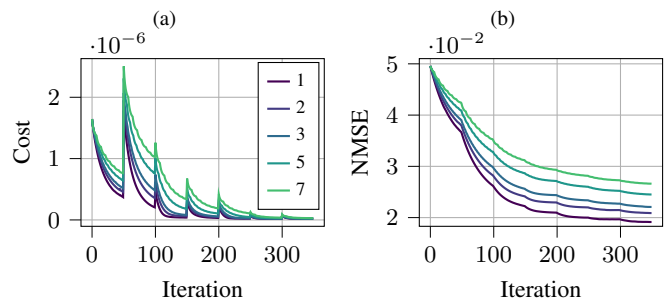FWI. Then, receivers are allowed to share data only, e.g., in every second, third, etc. iteration. To still perform updates on the subsurface image, each receiver uses the available gradients and subsurface models that were exchanged in the last exchange phase. These outdated data can still be sufficient to obtain suitable imaging results at the receivers depending on the exchange interval.

Fig. 4 shows cost and NMSE curves for a varying no. of exchange intervals. The higher the interval no. the less data is exchanged in the network. As expected, we observe that both cost and NMSE increase with a higher interval no. However, the algorithm is still able to converge to a suitable solution. This can be also seen in Fig. 3 which depicts imaging results for different exchange intervals. For higher intervals the contours of the anomalies are still clearly visible while the amplitudes within the ellipses decrease. Nevertheless, with intervals 2 or 3 we are still able to obtain good imaging results while cutting down the data exchange effectively by 50% and 66%, respectively.

C. Marmousi model

As a further numerical result we test our proposed method on the Marmousi model which is a well-known benchmark model in seismic imaging [17]. We select a subdomain of the Marmousi model and downscale the velocities to reduce computational complexity in the forward modeling step. We
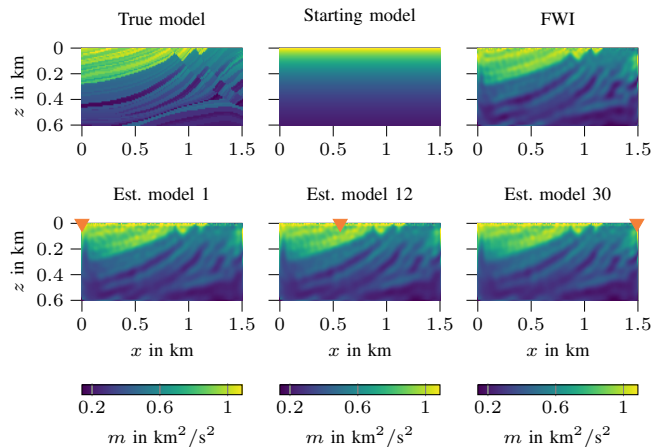
Fig. 5: First row: True model, starting model and FWI result for Marmousi model. Second row: Results by FD-ATCFWI with respective receiver position ▼.

Fig. 6: (a) Cost and (b) NMSE performance of FD-ATCFWI, FD-ATCFWI with full mesh and FWI for Marmousi model.

select a spacing of $\Delta x = \Delta z = 10\,\mathrm{m}$ which results in a physical domain of $1.5\,\mathrm{km} \times 0.6\,\mathrm{km}$. For the inversion, we employ $N_\mathrm{R} = 30$ receivers and $N_\mathrm{S} = 20$ sources evenly distributed over the surface. Furthermore, we select the frequencies to be in the range of 2 to $10\,\mathrm{Hz}$ with a frequency step of $\Delta f = 1\,\mathrm{Hz}$. For each frequency, we perform $N_\mathrm{FWI} = 40$ iterations. We select the steps size to be $\alpha^{[0]} = 0.05$ and again exponentially decrease it over the iterations. To initialize FWI and FD-ATCFWI, we use a simple velocity gradient that increases with depth.

Fig. 5 depicts the starting model and the reconstructed subsurface models using FD-ATCFWI and for reference FWI. We can clearly observe that the complex structure of the subsurface model is recovered well by FD-ATCFWI. In particular, over the displayed receivers the subsurface is equally well recovered. Compared to the centralized solution, no notable differences are visible in terms of imaging performance. However, compared to the ground truth model fine details and sharp contrasts present in the true subsurface are not recovered. Such details are more likely to be obtained when using regularizers such as the total variation norm that enables sharper edges in an image, cf. [15], [14]. Fig. 6 shows the cost as well as the NMSE over the iterations. It can be seen that FD-ATCFWI performs similar to FWI. Using a full mesh it achieves centralized performance.

V. Conclusion

We proposed a distributed full waveform inversion in the frequency domain for application in seismic multi-agent networks. In essence, FWI gradients obtained by the adjoint-state method and local subsurface estimates need to be exchanged among neighboring receivers. In numerical experiments, we demonstrated that centralized imaging performance is achieved by FD-ATCFWI over all receivers in the network independent of their position. Hence, with FD-ATCFWI we are able to obtain global subsurface information locally at receivers that would not be able to measure the required data at their 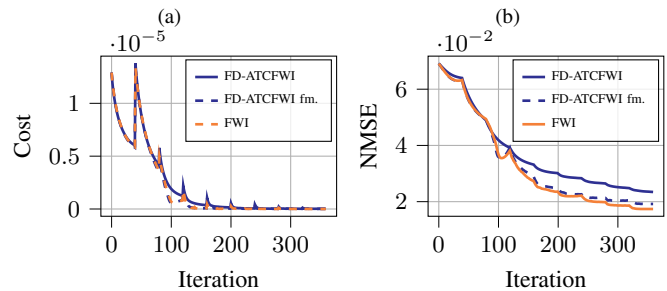specific position. To reduce data exchange in FD-ATCFWI we proposed to exchange data at certain intervals. We showed that FD-ATCFWI is still able to obtain high imaging quality despite reductions of 50% and 66% in data exchanges.

References

[1] F. Sauro, R. Pozzobon, M. Massironi *et al.*, "Lava tubes on Earth, Moon and Mars: A review on their size and morphology revealed by comparative planetology," *Earth-Science Reviews*, vol. 209, 2020.

[2] R. Lichtenheldt, E. Staudinger, S. Adeli *et al.*, "A mission concept for lava tube exploration on mars and moon –the dlr scout rover," in *Lunar and planetary Science Conference*, 2021.

[3] H. Kolvenbach, A. Mittelholz, S. C. Stähler *et al.*, "Lunarleaper - a mission concept to explore the lunar subsurface with a small-scale legged robot," in *IAC 2024 Conference Proceedings*, 2024.

[4] B.-S. Shin, D. Patel, L. Wientgens, D. Shutin, and A. Dekorsy, "Multi-agent 3d seismic exploration using adapt-then-combine full waveform inversion in a hardware-in-the-loop system," in *IEEE International Conference on Acoustics, Speech and Signal Processing*, Apr. 2024.

[5] J. Xue, J. Cheng, L.-J. Gelius *et al.*, "Full waveform inversion of transient electromagnetic data in the time domain," *IEEE Trans. Geosci. Remote Sens.*, vol. 60, pp. 1–8, 2022.

[6] D. Domenzain, J. Bradford, and J. Mead, "Joint full-waveform ground-penetrating radar and electrical resistivity inversion applied to field data acquired on the surface," *Geophysics*, vol. 87, no. 1, Nov. 2021.

[7] X. Wu, Y. Li, C. Su *et al.*, "Ultrasound computed tomography based on full waveform inversion with source directivity calibration," *Ultrasonics*, vol. 132, p. 107004, Jul. 2023.

[8] G. Kamath, L. Shi, W.-Z. Song, and J. Lees, "Distributed travel-time seismic tomography in large-scale sensor networks," *Journal of Parallel and Distributed Computing*, vol. 89, pp. 50–64, 2016.

[9] F. Li, M. Valero, Y. Cheng, T. Bai, and W. Z. Song, "Distributed sensor networks based shallow subsurface imaging and infrastructure monitoring," *IEEE Trans. Signal Inf. Process. Netw.*, vol. 6, 2020.

[10] S. Wang, F. Li, M. Panning, S. Tharimena, S. Vance, and W. Song, "Ambient noise tomography with common receiver clusters in distributed sensor networks," *IEEE Trans. Signal Inf. Process. Netw.*, vol. 6, 2020.

[11] B.-S. Shin and D. Shutin, "Joint distributed traveltime and full waveform tomography for enhanced subsurface imaging in seismic networks," *IEEE Trans. Comput. Imaging*, vol. 10, 2024.

[12] R. Clayton and B. Engquist, "Absorbing boundary conditions for acoustic and elastic wave equations," *Bulletin of the Seismological Society of America*, vol. 67, no. 6, 1977.

[13] R. E. Plessix, "A review of the adjoint-state method for computing the gradient of a functional with geophysical applications," *Geophys. J. Int.*, vol. 167, no. 2, 2006.

[14] E. Esser, L. Guasch, T. van Leeuwen, A. Y. Aravkin, and F. J. Herrmann, "Total variation regularization strategies in full-waveform inversion," *SIAM Journal on Imaging Sciences*, vol. 11, pp. 376–406, 2018.

[15] A. Kadu, H. Mansour, and P. T. Boufounos, "High-contrast reflection tomography with total-variation constraints," *IEEE Trans. Comput. Imag.*, vol. 6, 2020.

[16] A. H. Sayed, S. Tu, J. Chen, X. Zhao, and Z. J. Towfic, "Diffusion strategies for adaptation and learning over networks," *IEEE Signal Processing Magazine*, 2013.

[17] R. Versteeg, "The marmousi experience: Velocity model determination on a synthetic complex data set," *The Leading Edge*, 1994.